EUROPEAN ORGANIZATION FOR NUCLEAR RESEARCH

ELASTIC BACKWARD SCATTERING OF PIONS AND KAONS

W.F. Baker, P.J. Carlson, V. Chabaud and A. Lundby
CERN, Geneva, Switzerland

J. Banaigs, J. Berger, C. Bonnel, J. Duflo, L. Goldzahl and F. Plouin
Département Saturne, Saclay, France

ABSTRACT

The elastic scattering of π^+ mesons by protons near 180° has been measured at 2.85, 3.30, and 3.55 GeV/c, that of π^- mesons at 3.30 and 3.55 GeV/c, and that of K^+ and K^- mesons at 3.55 GeV/c. Steeply rising backward peaks are observed at all energies for π^+p scattering, whereas the π^-p angular distributions are not as steep. K^+p elastic scattering also shows a backward peak. No backward K^-p elastic scattering event was found. The upper limit (90% confidence) for the K^-p differential cross-section is twelve times smaller than the corresponding K^+p cross-section.

The behaviour of the differential cross-section close to 180° can be explained using direct channel resonances. The large ratio of the K^+p to K^-p cross-section can be understood in terms of baryon exchange.

Geneva - 2 December 1968
(Submitted to Nuclear Physics)

1. INTRODUCTION

The elastic scattering of $\pi^{\pm}$ and $K^{\pm}$ mesons by protons has been studied at angles between 160° and 180° (c.m.) in a spark chamber experiment at the CERN Proton Synchrotron (PS). Differential cross-sections were measured at incident momenta of 3.30 and 3.55 GeV/c for π^-p scattering, at 2.85, 3.30, and 3.55 GeV/c for π^+p scattering, and at 3.55 GeV/c for K^+p and K^-p scattering.

Elastic scattering above 2 GeV/c is dominated by a forward diffraction peak that is well known[1-6]. Prior to the experiment described here, a backward peak was observed in π^+p elastic scattering at 4 GeV/c [2], but little was known about its detailed shape. For π^-p and $K^{\pm}p$ scattering, only upper limits were measured[2,7].

The object of this experiment was to study in finer detail the backward scattering of π and K mesons by protons. Preliminary results have been previously published[8].

Section 2 presents details of the experimental apparatus. Section 3 describes the evaluation of the spark chamber photographs and details of the analysis. In Section 4 the results are presented and discussed. Conclusions are drawn in Section 5.

2. DESCRIPTION OF THE APPARATUS

In this experiment the backward scattering of mesons by protons was investigated using thin-plate optical spark chambers surrounding a liquid-hydrogen target. The directions of the incident and scattered mesons were measured, as were the direction and momentum of the forward-going recoil proton. A system of scintillation and Čerenkov counters was used to trigger the spark chambers. The layout of the apparatus is shown in Fig. 1. Through a system of mirrors all six spark chambers, SC_1-SC_6, were photographed stereoscopically by one camera. An additional spark chamber with transparent plates, SC_0, was used to study possible decays of the scattered mesons.

Scatterings at laboratory angles from 135° to 176° could be measured with this system. The relation between meson angle and proton angle is given in Fig. 2 for the momenta and mesons studied.

2.1 The triggering logic

The incident beam was defined by three scintillation counters S_1, S_2, S_3, and three threshold Čerenkov counters C_A, C_B, and C_C. After scattering in the hydrogen target, the backward-going meson was detected by one of the six scintillation counters S_4. The recoiling proton passed through the momentum-analysing magnet and was detected by one of the three scintillation counters S_5. The signals from these counters, after passing the fast logic circuitry, triggered the high voltage of the spark chambers.

In addition to these basic triggering counters, a number of counters were used in electronic anticoincidence to inhibit triggering of the chambers by unwanted processes. A set of scintillation counters S_7 surrounding the hydrogen target reduced the number of triggerings due to multi-prong inelastic events. A scintillation counter S_6 in the beam line but following the spark chambers reduced the number of accidental triggerings involving a beam particle that had traversed the system without interacting. A Čerenkov counter C_D, also located after the spark chambers, detected forward-going mesons and, in anticoincidence, inhibited triggering on forward scattering events.

A schematic diagram of the fast triggering electronics is given in Fig. 3. This provided the trigger to study backward K-meson scattering which is seen to be $S_1S_2S_3C_B\overline{(C_A + C_C + S_6)}\ S_4S_5\ \overline{(S_7 + C_D)}$. This trigger was used:

i) to fire the spark chamber high-voltage pulser, and to fire the discharge tube lamps in the fiducial marks and in the data box;

ii) to gate-off the fast electronics for 50 msec to allow the chambers to recover and the film in the camera to advance; and,

iii) to advance the film in the camera.

The typical triggering rate was one per PS burst in the K-meson scattering runs, and two to three in the pion scattering runs.

2.2 Scintillation and Čerenkov counters

The scintillation counters were made of plastic scintillator, and each was viewed by a 56 AVP photomultiplier tube through a lucite light-guide.

Three gas-filled threshold Čerenkov counters C_A, C_B, and C_C served to identify the masses of the incident particles. They were 1 m, 1 m, and 2 m long, respectively. C_A and C_C were filled with propane, and C_B with ethylene. When studying pion scattering, only C_A was used; its pressure was set so as to count pions, and it was placed in electronic coincidence with the three scintillation counters S_1, S_2, and S_3. For good discrimination against pions in the K-runs, all three threshold counters were used. Two, C_A and C_C, detected pions and were in anticoincidence with the third which counted both pions and kaons. The performance of this set of counters is indicated by the pressure curves shown in Fig. 4 for positive and negative beams at 3.55 GeV/c. The background below the K threshold consists of two parts:

i) knock-on electrons in C_B from protons that are not detected in C_A or C_C; this effect is pressure-dependent and is present for the positive beam only;

ii) muons between 2.0 and 2.5 GeV/c which are counted by C_B but not by C_A or C_C; these muons originate from decaying pions and constitute a small fraction of the beam.

The different background levels of these curves as well as their shapes can be explained by these two background processes. The effect of knock-on electrons depends on the type of gas and the pressure in C_B, but the effect due to muons depends on the conditions in C_A and C_C. The accidental coincidence rate in this system was determined by delaying the signal from C_B; it was found to be negligible. The rejection of pions as deduced from these curves was such that less than one pion in 10^3 was counted.

The Čerenkov counter C_D used to reject forward scattering events had a sensitive area of about 1 m^2, and was filled under pressure with propane. The Čerenkov light was collected by ten 58 AVP photomultiplier tubes. The counter detected pions with an efficiency of 88% with a background accidental rate of 0.6%. Details of its construction have been published[9].

2.3 The meson beam

About 10% of the internal circulating beam of the CERN Proton Synchrotron struck a cylindrical beryllium target of 1 mm diameter and 20 mm length. The internal beam consisted of approximately 7×10^{11} protons per burst at a

momentum of 19.2 GeV/c. Secondary particles produced in this target at an angle of 5.7° were transported to the experimental area by a system similar to one that has previously been described[10]. With this system, 3×10^5 particles per burst were obtained at momenta up to 3.8 GeV/c in a 1% momentum interval. Each burst of particles from the synchrotron lasted 250 msec and was repeated every 2.3 sec.

The beam of secondary particles was focused on the liquid-hydrogen target to a spot 40 mm wide and 25 mm high. The absolute value of the beam momentum was estimated to be known to ±50 MeV/c, whereas the momentum interval accepted was ±0.25%. The composition of the beam as determined by the Čerenkov counters is given in Table 1. At 3.55 GeV/c the ratio of muons to pions plus muons plus electrons was about 0.023. These muons had momenta between 2.0 and 3.55 GeV/c and arose mainly from decaying pions.

2.4 The liquid-hydrogen target

The hydrogen target unit consisted of a stainless-steel reservoir with a cylindrical mylar appendix which served as the target proper. This appendix was 57 cm long, 8 cm in diameter, and had 0.2 mm thick walls. Both reservoir and appendix were surrounded by thermal insulation consisting of fifty layers of 7 μm thick aluminized mylar. This, in turn, was surrounded by the aluminium vacuum container which had large, 0.2 mm thick, mylar windows in the region of the appendix. One charging of the reservoir was adequate enough to keep the target appendix full for twelve hours.

The target presented 4 g/cm^2 of hydrogen and 0.5 g/cm^2 of mylar to the beam.

2.5 Spark chambers and associated equipment

The six spark chambers SC_1-SC_6 each had six 1 cm gaps. The plates were of 25 μm aluminium foil and were glued to the lucite frames, which formed the walls of the chamber and through which the gaps were photographed. The sensitive area of each chamber was 40 × 104 cm^2, and was covered with a 190 μm sheet of mylar on each side. To prevent penetration of water vapour, a layer of 40 μm Kel-F was added to this. A gas recirculating system flushed the chambers continuously with a mixture of 65% neon and 35% helium (Henogal).

A 4500 V pulse was applied to alternate plates of the chamber to produce the sparks. Each set of two chambers was driven by one spark-gap pulser, and these in turn were driven by a 9000 V pulse from a master spark-gap. The capacitance of the high-voltage supply permitted six triggerings of the chambers per synchrotron burst with a voltage drop of less than 10%. The total time delay introduced by the pulsing units was approximately 50 nsec. A constant potential of 20 V, opposite in polarity to the high-voltage pulse, was maintained across the gaps to clear away residual ions following the spark discharge.

Each spark chamber was viewed horizontally as well as vertically, by means of a mirror mounted at 45° to the horizontal, to give a 90° stereo angle. In each view were placed for reference two fiducial crosses, each illuminated by two 10 cm long argon-filled flash tubes. A system of mirrors brought the two views of the six chambers together so that they could be recorded on one 35 mm film frame. A fast-cycling camera (Flight Research, Inc.), having a cycle time from 30 to 50 msec, permitted six photographs to be made per synchrotron burst. With an objective lens of 150 mm focal length, a demagnification of 58 was obtained. Perforated transparent Adox KB-17 film was used, having a speed of 40 ASA.

Additional information was recorded on each frame from a data box[11]. This box was of binary format, and each element was illuminated by a flash tube. These flash tubes together with those of the fiducial marks were triggered simultaneously with the spark chambers. In this way were recorded the run number, frame number, beam momentum and polarity, and the identity of the counters triggering the chambers for each particular event. A photograph of an elastic scattering is given in Fig. 5.

The additional spark chamber SC_0 had transparent plates and was viewed by a separate camera. This chamber has been described previously[12].

2.6 The analysing magnet

The large-gap magnet used to measure the momentum of the forward-going recoil proton had a cylindrically symmetric field with a bending power, $\int B\, d\ell$, of 1.5 Wb/m through the centre. Thus a typical recoil proton of momentum 3.5 GeV/c was deflected by 6.4°.

2.7 The acceptance of the system

The apparatus as shown in Fig. 1 detected scatterings at laboratory angles from 135° to 176°. This corresponded to centre-of-mass angles from about 163° to 179° depending on the incident momentum. The cut-off at 176° was due to interference with the incident beam and to the down-stream beam anticoincidence counter S_6. At any given scattering angle within this range, the geometrical efficiency was that fraction of the total azimuthal angle covered by the apparatus. This efficiency varied with the position of the scattering vertex and ranged from 8 to 25% in the useful volume of the target.

3. MEASUREMENTS AND DATA ANALYSIS

3.1 General

A total of 560,000 photographs were taken, of which we used 420,000 for our final results. In addition to these, test exposures were made with the liquid-hydrogen target empty or with the analysing magnet turned off. All films were scanned and measured by hand; some 20% were rescanned and remeasured to determine scanning and measuring efficiency.

3.2 Scanning criteria

Photographs showing one track going backward from the hydrogen target, together with a positively charged particle going forward, were selected. For some rolls, as many as 30% of the photographs contained two incident tracks. These were included in the selected sample, provided that the particle that came accidentally within the resolving time of the spark chambers ($\sim$ 1 μsec) passed through the whole set-up without interacting, thus making an easily recognizable "straight-through" track. The interacting probability was about 20%. Table 2 lists for each different run the number of films used, the number of candidates found in the scanning, as well as the number of elastic events finally accepted. The average speed for scanning was 500 frames per hour. A typical event is shown in Fig. 5.

3.3 The measurements

The photographs were measured on an x, y digitized measuring table with a least count of 0.1 mm. The images of each view of the six spark chambers were about a factor of 4 smaller on the table than in real space. For each

spark chamber four points were measured, these being the end-points of the tracks in each view. On each photograph four fiducial marks were measured. In addition, information from the data box was digitized.

A standard set of 24 fiducial marks was measured on 5 photographs. This was done on each film, mainly because spark chambers or fiducial marks might change position slightly.

The average speed for measuring was 10 pictures per hour. Approximately 10% of the measurements had to be redone because of faults in the measuring procedure.

3.4 Geometrical reconstruction and kinematical fit

The reconstruction of the tracks in the laboratory system was made in two steps in the computer program. The first step transformed the measured track in each view to a coordinate system relative to the two fiducials in that view. The second step transformed tracks to the laboratory system and correlated them in the two chambers of a telescope forming a telescope track. There were four telescopes: the incident, the scattered particle, the recoil proton, and the analysing magnet telescope. A three-prong vertex was calculated from the incident and scattered particle tracks. From the reconstructed tracks and the vertex, three quantities were calculated:

i) coplanarity ϕ, being the projection of the unit vector along the proton track on the normal to the plane defined by the incident and scattered meson;

ii) $\Delta\Theta_p$ defined from

$$\Delta\Theta_p = \Theta_p^{\text{measured}} - \Theta_p^{\text{calculated}} ,$$

where $\Theta_p^{\text{measured}}$ is the measured angle between the incident track and recoil proton track projected to the plane defined by the incident and scattered tracks;

iii) Δp_p defined from

$$\Delta p_p = p_p^{\text{measured}} - p_p^{\text{calculated}} ,$$

where p_p^{measured} is the measured value of the recoil proton momentum, obtained from the analysing magnet.

The magnet tracking program used a two-prong vertex formed by the incident and scattered meson and tracks before and after the magnet to identify the particle trajectory. The measured angle of the scattered particle was used to calculate both $\Theta_p^{calculated}$ and $p_p^{calculated}$. The distribution of Δp for the π^+ 2.85 GeV/c run is shown in Fig. 6. In approximately 20% of the events, the backward-scattered meson passed through the aluminium target supports. The distance traversed was typically 1-2 cm and caused multiple scattering and losses due to interactions. To refine the analysis, the events for each run were divided into two groups. Group 1 contained all events that did not pass through aluminium; group 2 contained events passing through aluminium. The standard deviations of the distributions of ϕ, $\Delta\Theta$, and Δp are listed in Table 3 for the two groups, averaged over all runs.

For each run, a χ^2 with 3 degrees of freedom was constructed:

$$\chi^2 = \left(\frac{\phi}{\sigma_\phi}\right)^2 + \left(\frac{\Delta\Theta}{\sigma_{\Delta\Theta}}\right)^2 + \left(\frac{\Delta p}{\sigma_{\Delta p}}\right)^2 .$$

In Fig. 7 is shown a χ^2 distribution obtained. Events with $\chi^2 > 11$, corresponding to a χ^2 probability of 1.2%, were rejected. The number of events found are listed in Table 2.

3.5 Identification of Kp elastic scatterings

At most, 1% of the incident particles labelled as K's were in fact pions (see Section 2.2). This could give rise to a contamination of a few π^+ events in our observed 22 K^+ events. However, by kinematical arguments we can show that our contamination is most likely zero.

Of those events obtained in the K^+-run, some will fulfil the kinematical criteria for both K^+ and π^+ backward scattering. For given incident momentum and laboratory angle of the backward going meson (Θ_m^{lab}) there is a difference in laboratory momentum of the recoil proton (p_p^{lab}) and in the laboratory angle of the recoil proton (Θ_p^{lab}) for the two hypotheses of K and π backward scattering. At an incident momentum of 3.55 GeV/c, the difference in recoil proton momentum is constant within 10% over the angular range covered in

this experiment, and amounts to 0.11 GeV/c compared to our experimental resolution of 0.13 GeV/c. Thus we cannot use the momentum measurement to distinguish the two hypotheses.

For given Θ_m^{lab}, the difference in Θ_p^{lab} for the two hypotheses is approximately a linear function of Θ_m^{lab}, and is 0° for $\Theta_m^{lab} = 180°$ and 1.1° for $\Theta_m^{lab} = 140°$. As our resolution in Θ_p^{lab} is 0.27°, there is an angular region where we can unambiguously distinguish between the two hypotheses. In Fig. 8 we have plotted the difference between the calculated and the measured values of Θ_p^{lab}, assuming K scattering. From the knowledge of the distribution of Θ_π^{lab} from the π-runs we conclude that the contamination of π events in our K^+ events is most likely to be zero and, with 95% confidence less than two events. This conclusion is further supported by the lack of π events in our K^--runs; therefore no subtraction of background arising from π events was made.

3.6 Cross-section calculations

The differential elastic cross-section for an interval $\Delta \cos \Theta^{c.m.}$ was calculated from the formulae

$$\frac{d\sigma}{d\Omega} = \frac{1}{2\pi \, \Delta \cos \Theta^{c.m.}} \cdot \frac{1}{N_t \cdot N_i} \cdot \sum_\nu \frac{1}{\varepsilon_\nu \ell_\nu}$$

and

$$\frac{d\sigma}{dt} = \frac{\pi}{(p^{c.m.})^2} \frac{d\sigma}{d\Omega} ,$$

where N_t = number of target protons per cm^3, taken to be 4.23×10^{22} protons/cm^3

N_i = number of incident particles (pions or kaons)

ε_ν = correction factor for particle losses

ℓ_ν = mean visible target length for event ν obtained by integration over the azimuthal angle of the event-plane around the incident track.

This can be shown to be an unbiased estimate of the differential cross-section[13].

The product $\varepsilon_\nu \ell_\nu$, i.e. the weighting of individual events, varies by a factor of 10 over the angular range included in the results.

3.7 Correction factors

Our final results have been corrected for the following:

i) Decays. This correction is typically 5% for π events and 30% for K events.

ii) Absorption and interaction in the hydrogen target, target walls and target supports, counters, spark chambers and air. This correction amounts to about 15%.

iii) Scanning efficiency. This correction varies from 0% to 15% depending on the scanner and the film quality.

iv) Photographs containing more than two incident tracks. The correction is 5% to 10% for π-runs, 20 to 30% for K-runs.

v) Recoil protons that are counted in the large Čerenkov counter C_D, thus eliminating the event electronically. This correction amounts to 8.7%

vi) Muons in the incident beam. This correction of 2.3% at 3.55 GeV/c, 3.0% at 3.30 GeV/c, and 3.8% at 2.85 GeV/c was applied to the π results only.

vii) Knock-on electrons hitting the set of anticounters surrounding the target or hitting the Čerenkov counter C_D. Correction of 0.5%.

viii) Administrative efficiency. This includes losses of events in the analysing chain as well as some losses due to false measurements. Correction of 4.3%.

ix) Inelastic background. This correction was obtained from the χ^2 distribution. Assuming a uniform background of inelastic events, no angular dependence of this background was found. It was smallest (about 4%) for the π^+-run at 2.85 GeV/c, and largest (about 10%) for the K^+-run.

4. RESULTS AND DISCUSSION

The differential cross-sections measured in this experiment are listed in Tables 4, 5, 6, and 7. The errors are one standard deviation and contain a statistical part (from the number of events observed) and a systematic part, added quadratically. The systematic part takes into account a relative error in the calculation of the geometrical efficiency over the angular range. In addition to the listed errors, there is an over-all normalization error of

±10%: for example, error in absolute beam momentum, approximations in the calculations of the visible lengths in hydrogen, absorption and decay corrections, faulty rejections in magnet tracking, uncertainty in the χ^2 parameters. To calculate $(d\sigma/d\Omega)/(d\sigma/d\Omega)_0$, the 0° differential cross-section was taken to be

$$\left(\frac{d\sigma}{d\Omega}\right)_0 = \frac{(p^{c.m.})^2}{16\pi\hbar^2c^2}\ \sigma^2_{tot}\ ,$$

where σ_{tot} is the total cross section[14,15].

The results have been plotted in Figs. 9 to 12. We have fitted the differential cross-section to an exponential in u

$$\frac{d\sigma}{du} = A \cdot e^{Bu}\ ,$$

where u is the four-momentum transfer squared between the incident meson and the outgoing proton, and is given by

$$u = \frac{(m_m^2 - m_p^2)^2}{s} - 2(p^{c.m.})^2\ (1 + \cos\theta_m^{c.m.}),$$

where m_m and m_p stand for the masses of the meson and proton, s is the total energy in the c.m. system squared, $p^{c.m.}$ is the momentum in the c.m. system, and $\theta_m^{c.m.}$ is the scattering angle of the meson in the c.m. system.

The results of the least squares fits are given in Table 8. The last two points are not included in the fit of the π^+ 2.85 GeV/c data. As can be seen from the χ^2 probabilities, our data can be well fitted by the exponential in u.

The π^+p angular distributions show steeply rising backward peaks. A comparison with the forward diffraction peak[1] which is well fitted to the form

$$\frac{d\sigma}{d|t|} = A \cdot e^{Bt}$$

(t is the four-momentum transfer squared between incident and outgoing meson) with a slope B = 6.7 0.2 $(GeV/c)^{-2}$ [1], shows that the backward peaks at 3.30 and 3.55 GeV/c are significantly steeper. Recent data at

higher energies[16] show clearly that the backward peak in π^+p elastic scattering shrinks with increasing energy. This is illustrated in Fig. 13, where the slope B is plotted as a function of s.

The π^-p angular distributions are more flat than the corresponding π^+p distributions. Combined with data at smaller scattering angles[1] the π^-p angular distributions show backward peaks.

The measured differential cross-section of K^+p backward elastic scattering gives, together with other published data at smaller scattering angles[17], the evidence for a backward peak in K^+p elastic scattering. This has recently been confirmed at an incident momentum of 3.53 GeV/c [18]. The measured upper limit for the Kp differential cross-section is lower than has been measured previously[19], and the resulting ratio of the K^+p to K^-p differential cross-section close to 180° is greater than 12.

4.1 Models for backward scattering

Recently various models have been proposed for backward scattering interactions with contributions from the direct and the crossed channel[20]. This is illustrated in Fig. 14 for meson-proton backward scattering. The direct channel contribution is the formation and subsequent decay of a resonance in the mp system, where m stands for the incident meson. The crossed channel contribution is the exchange of a baryon with suitable quantum numbers. In Table 9 are listed resonances that may contribute to $\pi^\pm$ and $K^\pm$ backward scattering.

In the K^+p system there is no well-established resonance. Structures have been seen in a K^+p and K^+n total cross-section experiment[21], but their interpretation as resonances is not obvious[22]. Even if these structures were taken to be resonances, their elasticities would be too small to produce the relatively large K^+p backward differential cross-section found in this experiment. It is more attractive to interpret our kaon data as evidence of baryon exchange in the crossed channel. The existence of negative strangeness baryons permits backward K^+p scattering, whereas the lack of positive strangeness baryons prohibits backward K^-p scattering in agreement with our results.

Backward peaks for $\pi^\pm p$ scattering can be generated through both channels It is believed that the baryon exchange would dominate over the direct channel contributions for very high energies, whereas the low-energy data would be dominated by the contributions from the direct channel.

In order to parametrize the contributions from the direct channel we can write the differential cross-section

$$\frac{d\sigma}{d\Omega} = |f|^2 + |g|^2 \sin^2 \Theta \ .$$

When expanding into partial waves we have for the non-spin-flip amplitude

$$f = \frac{1}{p^{c.m.}} \sum_{\ell,J} (J + \tfrac{1}{2}) f_\ell^J \, P_\ell \, (\cos \Theta)$$

and for the spin-flip amplitude

$$g = \frac{1}{p^{c.m.}} \sum_{\ell,J} (-1)^{J-\ell+\frac{1}{2}} \, f_\ell^J \, P'_\ell \, (\cos \Theta) \ ,$$

where $P'_\ell(\cos \Theta) = d/d \cos \Theta \, P_\ell(\cos \Theta)$ with J and ℓ as total and orbital angular momenta of the resonance, respectively. P_ℓ is the Legendre function. At 180° we have

$$f = \frac{1}{p^{c.m.}} \sum_{\ell,J} (J + \tfrac{1}{2}) \, (-1)^\ell \, f_\ell^J$$

$$g \sin \Theta = 0 \ .$$

Due to the factor $(-1)^\ell$, a random distribution of background partial waves would then tend to cancel. The contribution from a single resonance or a sum of resonances with the same parity $(-1)^{\ell+1}$ results in a backward peak. As energy increases there is a shift in the population of resonances to higher ℓ and we therefore get sharper backward peaks.

If we give the partial wave amplitude the Breit-Wigner form

$$f_\ell^J = \frac{x}{\varepsilon - i} \ , \qquad \varepsilon = \frac{M^2 - s}{M\Gamma} \ ,$$

where M, Γ, and x stand for the mass, full width, and elasticity of the resonance, respectively, we can calculate the differential cross-section. The momentum dependence of the differential cross-section at 180° calculated in this way[24,25] is in good agreement with experimental data. We have calculated in a similar way the angular distribution for $\pi^{\pm}p$ backward scattering, and the result for $\pi^{+}p$ at 2.85 GeV/c is compared to the data in Fig. 9. The resonance parameters used are listed in Table 10. It is seen that pion scattering very near 180° can be parametrized in terms of direct channel contributions.

5. CONCLUSIONS

i) The large lower limit of the ratio of the differential cross-sections for $K^{+}p$ and $K^{-}p$ close to 180° supports the baryon exchange mechanism. $K^{+}p$ elastic scattering exhibits a backward peak.

ii) The magnitude of the differential cross-section for $\pi^{\pm}p$ close to 180° and its energy dependence is qualitatively understood in terms of direct channel resonances. However, an explanation of the angular distributions is more complex, and other mechanisms are likely to contribute. $\pi^{+}p$ backward scattering shows steeply rising backward peaks, whereas the $\pi^{-}p$ angular distributions are more nearly flat.

Acknowledgements

We wish to thank Dr. E.G. Michaelis and Prof. F. Schmidt for their participation in the initial phase of this work. We thank P. Anzoli, R. Kiesler, B. Mouellic, D. Ploujoux and R. Stöckli for their technical assistance.

Table 1

Beam composition at 3.55 GeV/c

Particle	Beam composition in % at 3.55 GeV/c	
	Negative beam	Positive beam
p	0.5	29.2
K	1.7	2.7
$\pi + \mu + e$	97.8	68.1

Table 2

Statistics on data taking

Incident particle	Incident momentum GeV/c	Number of photographs taken	Number of elastic candidates	Number of elastic events accepted
π^+	2.85	30,000	1304	650
π^+	3.30	24,000	600	170
π^-	3.30	45,000	298	112
π^+	3.55	87,000	1731	720
π^-	3.55	129,000	1048	352
K^+	3.55	54,000	110	22
K^-	3.55	51,000	30	0

Table 3

Standard deviations for the distribution of ϕ, $\Delta\Theta$ and Δp

Group	Standard deviation		
	ϕ mrad	$\Delta\Theta$ mrad	Δp GeV/c
1 (non-Al)	6.2	5.2	0.13
2 (Al)	9.8	6.1	0.14

Table 4

Differential cross-sections at 2.85 GeV/c

$p^{c.m.} = 1.07$ GeV/c, $s = 6.25$ (GeV)^2

Particle	$\cos\Theta_\pi^{c.m.}$	$\Delta\cos\Theta$	$-t$ (GeV/c)^2	u (GeV/c)^2	No. of events	$d\sigma/d\Omega$ μb/sr	$d\sigma/du$ μb/(GeV/c)^2	$\frac{d\sigma}{d\Omega}\Big/\left(\frac{d\sigma}{d\Omega}\right)_0 \times 10^3$
π^+	-0.995	0.004	4.562	0.107	144	168 ± 15	460 ± 41	10.02
	-0.991	0.004	4.553	0.098	137	152 ± 14	416 ± 37	9.07
	-0.987	0.004	4.543	0.089	115	142 ± 14	390 ± 38	8.50
	-0.983	0.004	4.534	0.080	88	134 ± 15	368 ± 41	8.02
	-0.979	0.004	4.525	0.070	63	122 ± 16	336 ± 43	7.31
	-0.975	0.004	4.516	0.061	46	117 ± 18	321 ± 48	6.98
	-0.971	0.004	4.507	0.052	34	113 ± 20	309 ± 54	6.74
	-0.967	0.004	4.498	0.043	16	70 ± 18	192 ± 48	4.18
	-0.963	0.004	4.489	0.034	7	39 ± 15	108 ± 41	2.36

Table 5

Differential cross-sections at 3.30 GeV/c
$p^{c.m.} = 1.16$ GeV/c, $s = 7.10$ (GeV)^2

Particle	$\cos\theta_\pi^{c.m.}$	$\Delta\cos\theta_\pi^{c.m.}$	$-t$ (GeV/c)^2	u (GeV/c)^2	No. of events	$\frac{d\sigma}{d\Omega}$ μb/sr	$\frac{d\sigma}{du}$ μb/(GeV/c)^2	$\frac{d\sigma}{d\Omega}/\left(\frac{d\sigma}{d\Omega}\right)_0$ $\times 10^3$
π^-	-0.995	0.008	5.389	0.091	46	10.6 ± 1.6	24.7 ± 3.7	0.47
	-0.987	0.008	5.368	0.069	33	10.1 ± 1.8	23.4 ± 4.1	0.45
	-0.979	0.008	5.346	0.048	18	8.2 ± 1.9	19.0 ± 4.5	0.36
	-0.971	0.008	5.324	0.026	9	7.7 ± 2.6	17.8 ± 6.0	0.34
	-0.963	0.008	5.303	0.005	6	6.4 ± 2.6	14.9 ± 6.1	0.28
π^+	-0.994	0.006	5.386	0.088	64	58.1 ± 7.5	135.2 ± 17.5	3.29
	-0.988	0.006	5.370	0.072	46	45.8 ± 5.9	106.5 ± 13.7	2.59
	-0.982	0.006	5.354	0.056	28	34.4 ± 6.6	80.0 ± 15.3	1.95
	-0.976	0.006	5.338	0.040	15	25.5 ± 6.6	59.4 ± 15.4	1.44
	-0.970	0.006	5.322	0.023	10	24.7 ± 7.8	57.5 ± 18.3	1.40
	-0 964	0.006	5.305	0.007	7	23.3 ± 8.8	54.1 ± 20.5	1.32

Table 6

Differential cross-sections at 3.55 GeV/c

$p^{c.m.} = 1.21$ GeV/c, $s = 7.57$ (GeV)^2

Particle	$\cos \Theta_\pi^{c.m.}$	$\Delta \cos \Theta_\pi^{c.m.}$	$-t$ (GeV/c)^2	u (GeV/c)^2	No. of events	$\frac{d\sigma}{d\Omega}$ μb/sr	$\frac{d\sigma}{du}$ μb/(GeV/c)^2	$\frac{d\sigma}{d\Omega}\Big/\left(\frac{d\sigma}{d\Omega}\right)_0$ × 10^3
π^-	-0.997	0.004	-5.856	0.089	80	9.6 ± 1.1	20.5 ± 2.4	0.40
	-0.993	0.004	-5.844	0.077	60	7.9 ± 1.0	16.9 ± 2.2	0.33
	-0.989	0.004	-5.833	0.066	54	8.5 ± 1.2	18.3 ± 2.5	0.36
	-0.985	0.004	-5.821	0.054	38	7.1 ± 1.2	15.3 ± 2.5	0.30
	-0.981	0.004	-5.809	0.042	29	6.6 ± 1.2	14.1 ± 2.6	0.27
	-0.977	0.004	-5.797	0.030	29	8.6 ± 1.6	18.5 ± 3.5	0.36
	-0.973	0.004	-5.786	0.019	21	8.3 ± 1.8	17.8 ± 3.9	0.35
	-0.969	0.004	-5.774	0.007	10	5.0 ± 1.6	10.6 ± 3.4	0.21
	-0.965	0.004	-5.762	-0.005	14	9.9 ± 2.7	21.2 ± 5.7	0.41
	-0.961	0.004	-5.751	-0.016	11	9.5 ± 2.9	20.4 ± 6.2	0.40
	-0.957	0.004	-5.739	-0.028	6	9.3 ± 3.8	20.0 ± 8.2	0.39
π^+	-0.995	0.004	5.850	0.083	190	59.0 ± 4.6	126.4 ± 9.8	3.12
	-0.991	0.004	5.839	0.072	154	50.4 ± 4.3	108.0 ± 9.2	2.66
	-0.987	0.004	5.827	0.060	122	45.2 ± 4.3	96.8 ± 9.2	2.39
	-0.983	0.004	5.815	0.048	74	31.9 ± 3.8	68.4 ± 8.2	1.68
	-0.979	0.004	5.803	0.036	60	31.6 ± 4.2	67.8 ± 9.0	1.67
	-0.975	0.004	5.792	0.025	35	23.5 ± 4.0	50.3 ± 8.6	1.24
	-0.971	0.004	5.780	0.013	42	36.4 ± 5.7	78.1 ± 12.2	1.92
	-0.967	0.004	5.768	0.001	17	19.4 ± 4.7	41.6 ± 10.2	1.02
	-0.963	0.004	5.756	-0.011	15	23.7 ± 6.2	50.8 ± 13.2	1.25
	-0.959	0.004	5.745	-0.022	7	14.9 ± 5.7	32.0 ± 12.1	0.79
	-0.955	0.004	5.733	-0.034	4	11.9 ± 5.9	25.4 ± 12.7	0.63

Table 7

Differential cross-sections at 3.55 GeV/c.

The upper limit quoted for K^- corresponds to a 90% confidence upper limit.

$p^{c.m.} = 1.19$ GeV/c, $s = 7.85$ (GeV)^2

Particle	$\cos\Theta_K^{c.m.}$	$\Delta\cos\Theta$	$-t$ (GeV/c)^2	u (GeV/c)^2	No. of events	$\frac{d\sigma}{d\Omega}$ μb/sr	$\frac{d\sigma}{du}$ μb/(GeV/c)^2	$\frac{d\sigma}{d\Omega}\Big/\left(\frac{d\sigma}{d\Omega}\right)_0$ × 10^3
K^-	-0.9875	0.021	5.618	0.016	0	< 1.4	< 3.2	< 0.1
K^+	-0.9940	0.008	5.636	0.035	15	21.3 ± 5.9	47.4 ± 13.1	2.92
	-0.9835	0.013	5.607	0.005	7	14.9 ± 5.8	33.1 ± 12.9	2.06
K^+ (average)	-0.9875	0.021	5.618	0.016	22	17.3 ± 4.1	38.6 ± 9.1	2.39

Table 8

Fit of the differential cross-section to the form $d\sigma/du = A \cdot e^{Bu}$.

The value of B for K^+ backward scattering is a 70% confidence range obtained from a maximum likelihood estimate.

	B (GeV/c)$^{-2}$	A μb(GeV/c)^2	A μb/sr	$\frac{d\sigma}{du}_{180°}$ μb/(GeV/c)^2	$\frac{d\sigma}{d\Omega}_{180°}$ μb/sr	$P(\chi^2 > \chi^2)_{obs.}$
π^+ 2.85	7.6 ± 2.5	201 ± 45	73 ± 16	493 ± 44	179 ± 16	0.9
3.30	13.6 ± 3.4	40 ± 10	17 ± 4	164 ± 24	71 ± 10	0.9
3.55	11.3 ± 1.5	48 ± 4	22 ± 2	144 ± 11	67 ± 5	0.9
π^- 3.30	5.7 ± 3.8	15 ± 4	6 ± 2	27 ± 5	12 ± 2	0.9
3.55	0.9 ± 1.7	17 ± 2	8 ± 1	18 ± 2	8 ± 1	0.6
K^+ 3.55	0 < B < 27	31 ± 15	14 ± 7	58 ± 29	26 ± 13	-

Table 9

Contributions to backward scattering.
For nomenclature and details see Barash-Schmidt et al.[23].

Reaction	Direct channel	Crossed channel
$\pi^- p$	Δ, N	Δ
$\pi^+ p$	Δ	Δ, N
$K^- p$	Σ, Λ	Z?
$K^+ p$	Z?	Σ, Λ

Table 10

Parameters for resonances used in the
direct channel calculation.

Resonance mass in MeV/c^2	Spin-Parity J^P	Width MeV/c^2	Elasticity
$\Delta_\delta(1236)$	$3/2^+$	120	1
$\Delta_\beta(1670)$	$1/2^-$	180	0.4
$\Delta_\delta(1924)$	$7/2^+$	170	0.4
$\Delta_\delta(2450)$	$11/2^+$	280	0.105
$\Delta_\delta(2840)$	$15/2^+$	400	0.05
$\Delta_\delta(3220)$	$19/2^+$	440	0.01

REFERENCES

1) C.T. Coffin, N. Dikmen, L. Ettlinger, D. Meyer, A. Saulys, K. Terwilliger and D. Williams, Phys. Rev. 159, 1169 (1967).

2) Aachen-Berlin-Birmingham-Bonn-Hamburg-London-Munich Collaboration, Physics Letters 10, 248 (1964); Nuovo Cimento 31, 729 (1964).

3) D. Harting, P. Blackall, B. Elsner, A.C. Helmholz, W.C. Middelkoop, B. Powell, B. Zacharov, P. Zanella, P. Dalpiaz, M.N. Focacci, S. Focardi, G. Giacomelli, L. Monari, J.A. Beaney, R.A. Donald, P. Mason, L.W. Jones and D.O. Caldwell, Nuovo Cimento 38, 60 (1965).

4) E.H. Bellamy, T.F. Buckley, R.W. Dobinson, P.V. March, J.A. Strong, R.N.F. Walker, W. Busza, B.G. Duff, D.A. Garbutt, F.F. Heymann, C.C. Nimmon, K.M. Potter and T.P. Swetman, Phys. Rev. Letters 19, 476 (1967).

5) M.L. Perl, L.W. Jones and C.C. Ting, Phys. Rev. 132, 1252 (1963).

6) M.L. Perl, Y.Y. Lee and E. Marquit, Phys. Rev. 138 B, 707 (1965).

7) R. Crittenden, H.J. Martin, W. Kernan, L. Leipuner, A.C. Li, F. Ayer, L. Marshall and M.L. Stevenson, Phys. Rev. Letters 12, 429 (1964).

8) W.F. Baker, P.J. Carlson, V. Chabaud, A. Lundby, E.G. Michaelis, J. Banaigs, J. Berger, C. Bonnel, J. Duflo, L. Goldzahl and F. Plouin, Physics Letters 23, 605 (1966); 24 B, 317 (1967); 25 B, 361 (1967).

9) J. Banaigs, J. Berger, L. Goldzahl and B. Mouellic, Nucl.Instrum. Methods 48, 64 (1967).

10) M. Barbier, J.D. Dowell, P.I.P. Calmus, B. Leontic, A. Lundby, R. Meunier, G. Petrucci, L. Solinas, J.P. Stroot and M. Szeptycka, Nucl.Instrum. Methods 20, 66 (1963).

11) A Flash-Lamp Data Display system, A. Lang, CERN NP Electronics Group, Note 64-1 (1964).

12) J. Banaigs, J. Duflo, L. Goldzahl, B. Mouellic, C. Delorme, R. Kiesler and E.G. Michaelis, Nucl.Instrum. Methods 26, 137 (1964).

13) V. Chabaud, Thesis, 1968.

14) A. Citron, W. Galbraith, T.F. Kycia, B.A. Leontic, R.H. Phillips, A. Rousset and R.H. Sharp, Phys. Rev. 144, 1101 (1966).

15) R.J. Abrams, R.L. Cool, G. Giacomelli, T.F. Kycia, B.A. Leontic, K.K. Li and D.N. Michael, Phys. Rev. Letters 19, 678 (1967); 19, 259 (1967).

16) A. Ashmore, C.J.S. Damerell, W.R. Frisken, R. Rubenstein, J. Orear, D.P. Owen, F.C. Peterson, A.L. Read, D.G. Ryan and D.H. White, Phys. Rev. Letters 19, 460 (1967).

17) W. de Baere, J. Debaisieux, P. Dufour, F. Grard, D. Heughebaert, L. Pape, P. Peeters, F. Verbeure, R. Windmolders, R. George, Y. Goldschmidt-Clermont, V.P. Henri, B. Jongejans, D.W.G. Leith, A. Moisseev, F. Muller, J.M. Perreau and V. Yarba, Nuovo Cimento 45, 885 (1966).

18) D. Cline, C. Moore and D. Reeder, Phys. Rev. Letters 19, 675 (1967).

19) J. Gordon, Physics Letters 21, 117 (1966).

20) These models have been described in a review by M. Derrick, Proc. of the Topical Conf. on High-Energy Collisions of Hadrons, CERN Report 68-7 (1968), p. 111.

21) R.L. Cool, G. Giacomelli, T.F. Kycia, B.A. Leontic, K.K. Li, A. Lundby and J. Teiger, Phys. Rev. Letters 17, 102 (1966).

22) G. Goldhaber, Proc. Int. Conf. on Particles and Fields Rochester, (1967) (Interscience Publishers, N.Y., 1967), p. 57.

23) N. Barash-Schmidt, A. Barbaro-Galtieri, L.R. Price, M. Roos, A.H. Rosenfeld, P. Söding and C.G. Wohl, UCRL-8030, Aug. 1968 version (preprint).

24) F.N. Dikmen, Phys. Rev. Letters 18, 798 (1967),

25) A.S. Carroll, J. Fischer, A. Lundby, R.H. Phillips, C.L. Wang, F. Lobkowicz, A.C. Melissinos, Y. Nagashima and S. Tewksbury, Phys. Rev. Letters 20, 607 (1968).

Figure captions

Fig. 1 : Experimental layout. The incident beam enters from the right.

Fig. 2 : Elastic scattering kinematics.

Fig. 3 : Pressure curves obtained with positive beam at 3.55 GeV/c. 123 represents a threefold coincidence $S_1S_2S_3$. C_A and C_C contained propane with a pressure of 3 bar. C_B contained ethylene.

Fig. 4 : Block diagram of electronics.

Fig. 5 : A backward elastic scattering event. From left to right the two views of the spark chambers SC_1 to SC_6. On top, the horizontal view. The first two chambers show the incident and backward scattered meson, the third and fourth chambers show the recoil proton before the bending magnet, and the last two chambers show the recoil proton after the bending magnet. The data box is displayed between the horizontal view of chambers 4 and 5.

Fig. 6 : The distribution of Δp for the π^+ 2.85 GeV/c run. FWHM $\approx$ 0.25 GeV/c corresponding to about 8% of the momentum.

Fig. 7 : χ^2 distribution obtained for the π^+ 2.85 GeV/c run.

Fig. 8 : Θ_p (measured) - Θ_p (calculated) as a function of Θ^{lab}_{meson} for the 22 elastic scattering events found in the K^+-run at 3.5 GeV/c.

Fig. 9 : Angular distribution of π^+p backward scattering at 2.85 GeV/c. Also shown is a fit to the experimental data and a calculated angular distribution (see Section 4).

Fig. 10 : Angular distribution of πp backward scattering at 3.30 GeV/c. Straight lines are fits to the experimental data.

Fig. 11 : Angular distribution of πp backward scattering at 3.35 GeV/c. Straight lines are fits to the experimental data.

Fig. 12 : Differential cross-section of Kp backward scattering at 3.55 GeV/c. Data from this experiment and from Ref. 18.

Fig. 13 : The slope of the backward peak in π^+p elastic scattering as a function of s. Data from this experiment and from Ref. 16.

Fig. 14 : Diagram to illustrate the different contributions to backward scattering.

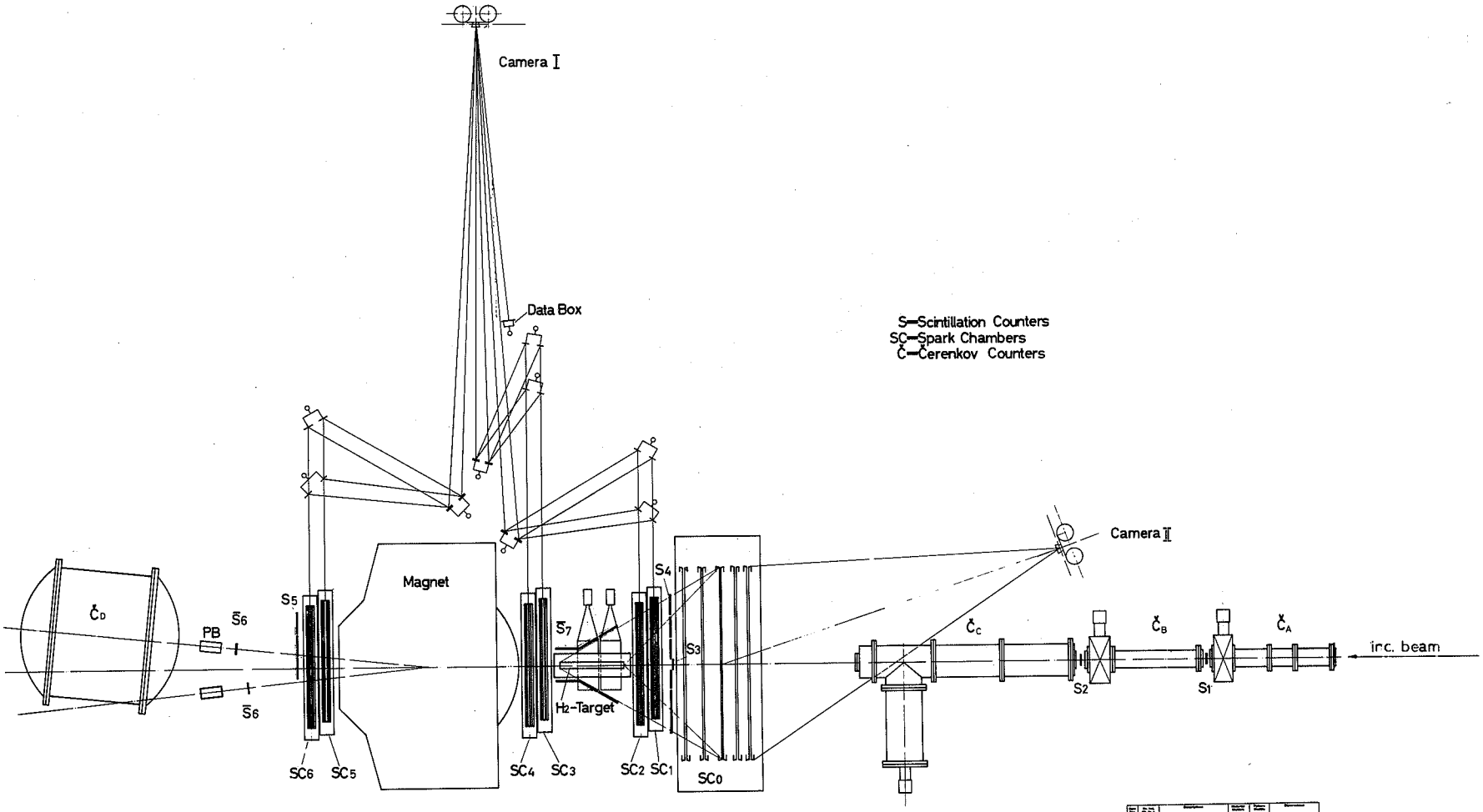
Camera I
Data Box
S—Scintillation Counters
SC—Spark Chambers
Č—Cerenkov Counters
Camera II
Magnet
PB
S5
S6
S6
S7
S4
S3
S2
S1
H2-Target
inc. beam
SC6
SC5
SC4
SC3
SC2
SC1
SC0
Č_D
Č_C
Č_B
Č_A
π-p Scattering
Layout of Experiment
1:10
CERN-NP
GENÈVE
LUNDBY-IVRY

Fig. 1

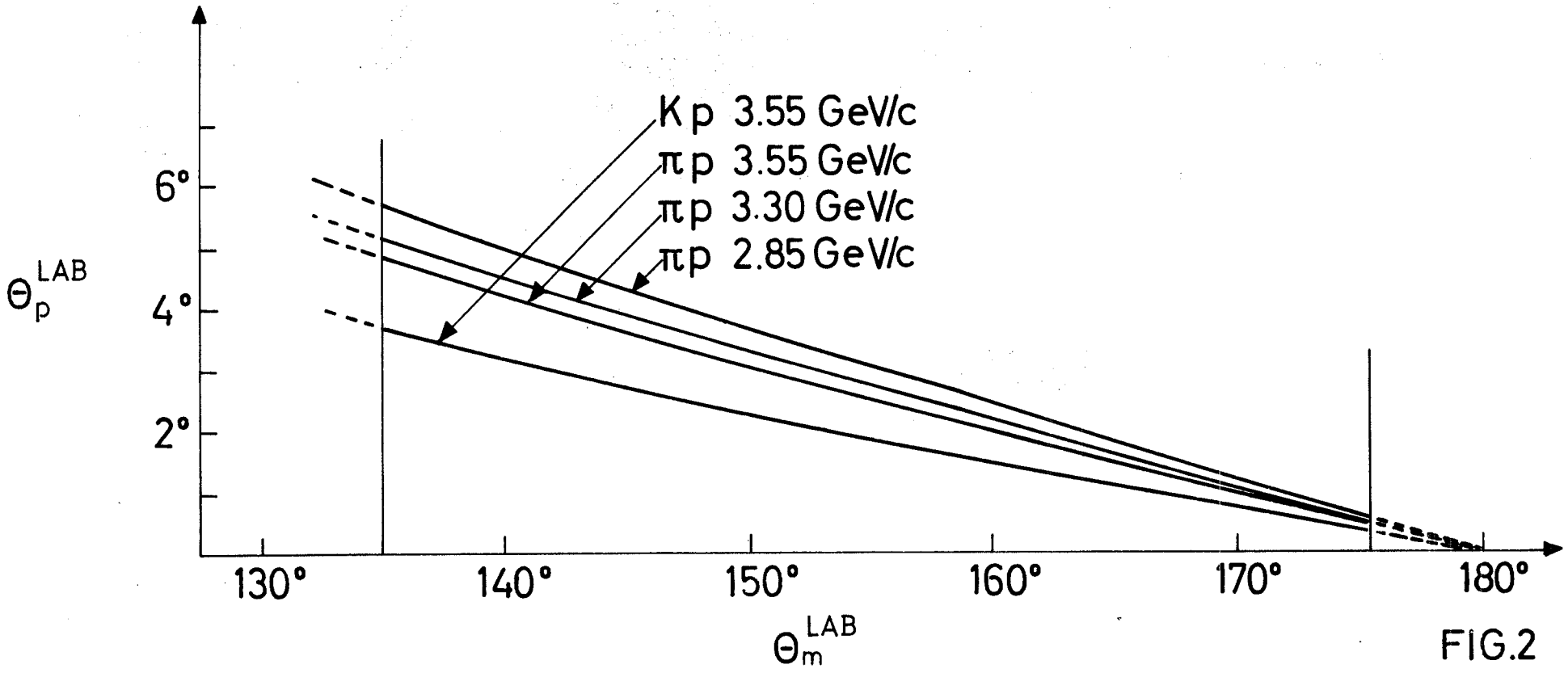
K p 3.55 GeV/c
π p 3.55 GeV/c
π p 3.30 GeV/c
π p 2.85 GeV/c
Θ_p^{LAB}
6°
4°
2°
130°
140°
150°
160°
170°
180°
Θ_m^{LAB}

FIG.2

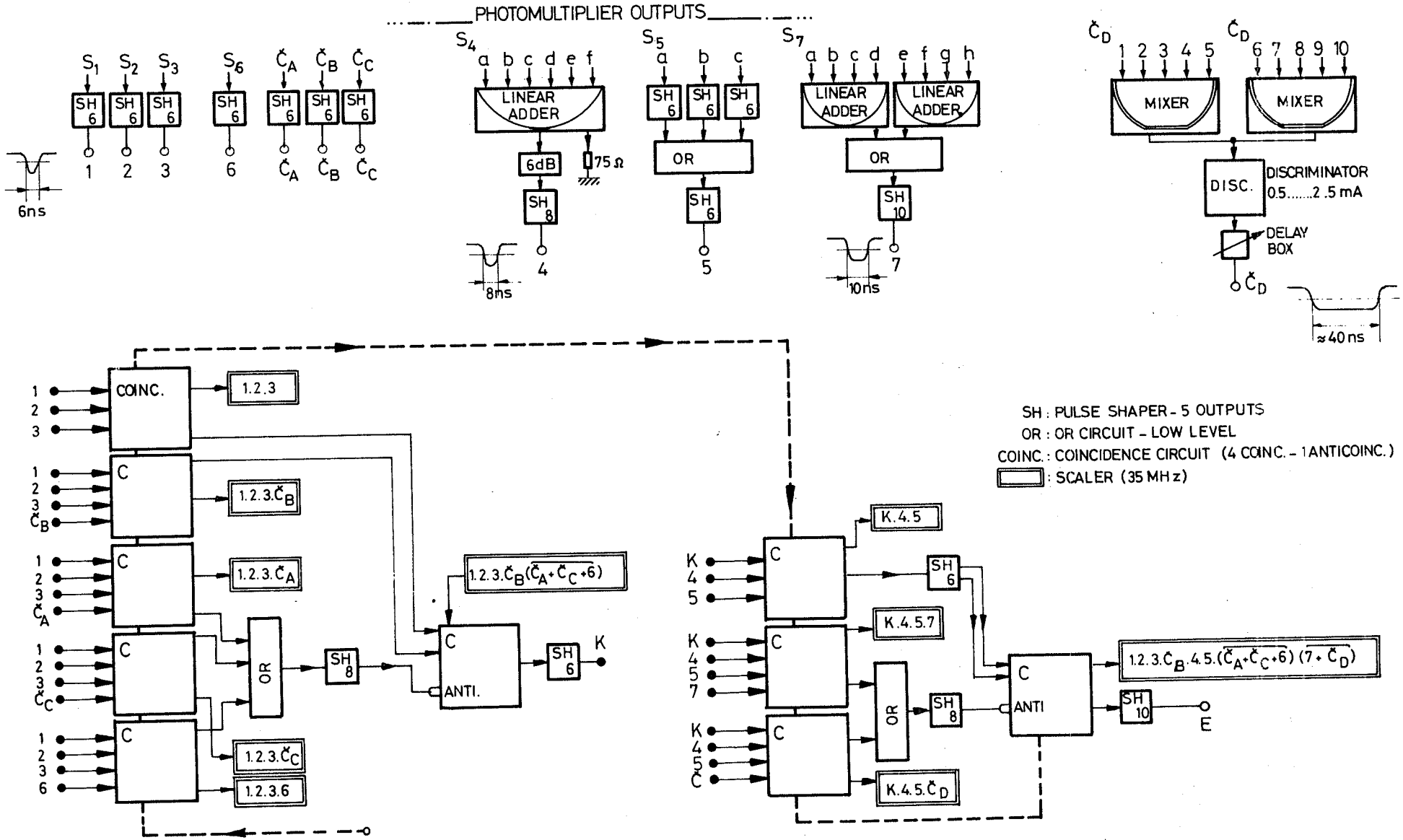
PHOTOMULTIPLIER OUTPUTS
S1 S2 S3 S6 ČA ČB ČC
SH 6
1 2 3 6 ČA ČB ČC
6ns
S4 a b c d e f
LINEAR ADDER
6dB
75 Ω
SH 8
4
8ns
S5 a b c
SH 6
OR
SH 6
5
S7 a b c d e f g h
LINEAR ADDER
LINEAR ADDER
OR
SH 10
7
10ns
ČD 1 2 3 4 5
ČD 6 7 8 9 10
MIXER
MIXER
DISC.
DISCRIMINATOR
0.5.....2.5 mA
DELAY BOX
ČD
≈40 ns
SH : PULSE SHAPER - 5 OUTPUTS
OR : OR CIRCUIT - LOW LEVEL
COINC. : COINCIDENCE CIRCUIT (4 COINC. - 1 ANTICOINC.)
: SCALER (35 MHz)
COINC.
1.2.3
C
1.2.3.ČB
1.2.3.ČA
1.2.3.ČB(ČA+ČC+6)
OR
SH 8
ANTI.
SH 6
K
1.2.3.ČC
1.2.3.6
K.4.5
SH 6
K.4.5.7
OR
SH 8
ANTI
1.2.3.ČB.4.5.(ČA+ČC+6)(7+ČD)
SH 10
E
K.4.5.ČD

FIG. 3

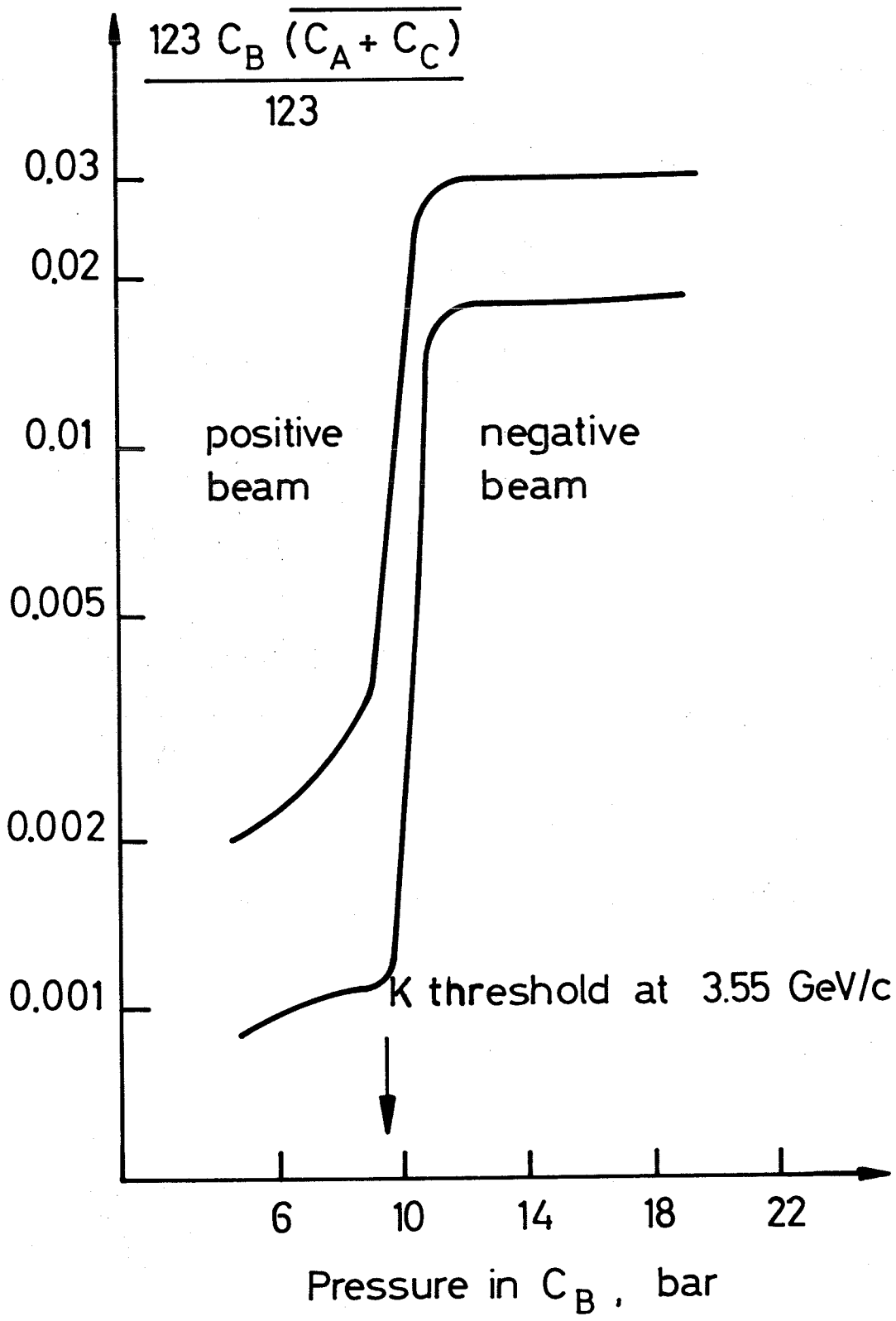
$\frac{123\ C_B\ \overline{(C_A + C_C)}}{123}$
0.03
0.02
0.01
0.005
0.002
0.001
positive beam
negative beam
K threshold at 3.55 GeV/c
6
10
14
18
22
Pressure in C_B, bar

Fig. 4

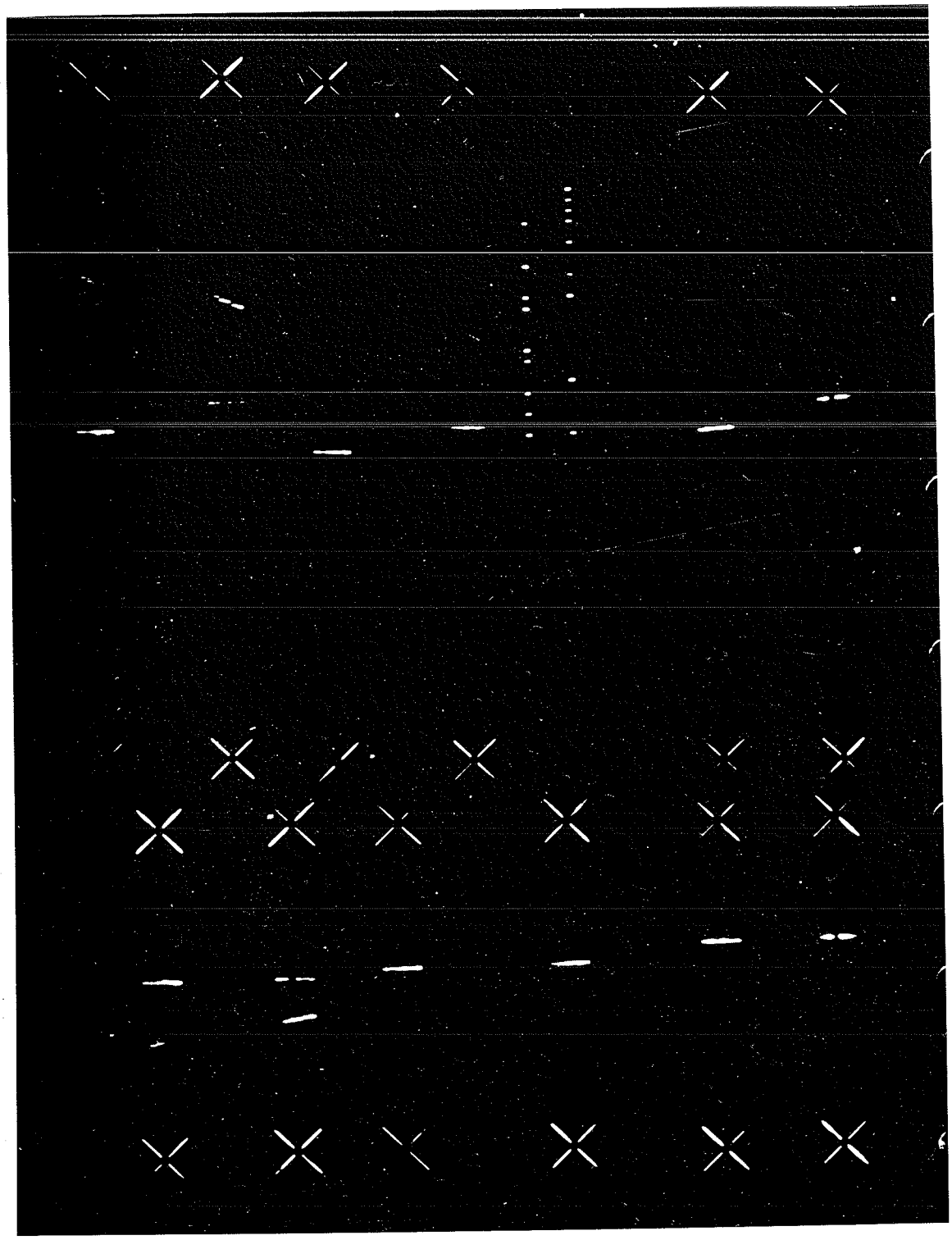

Fig. 5

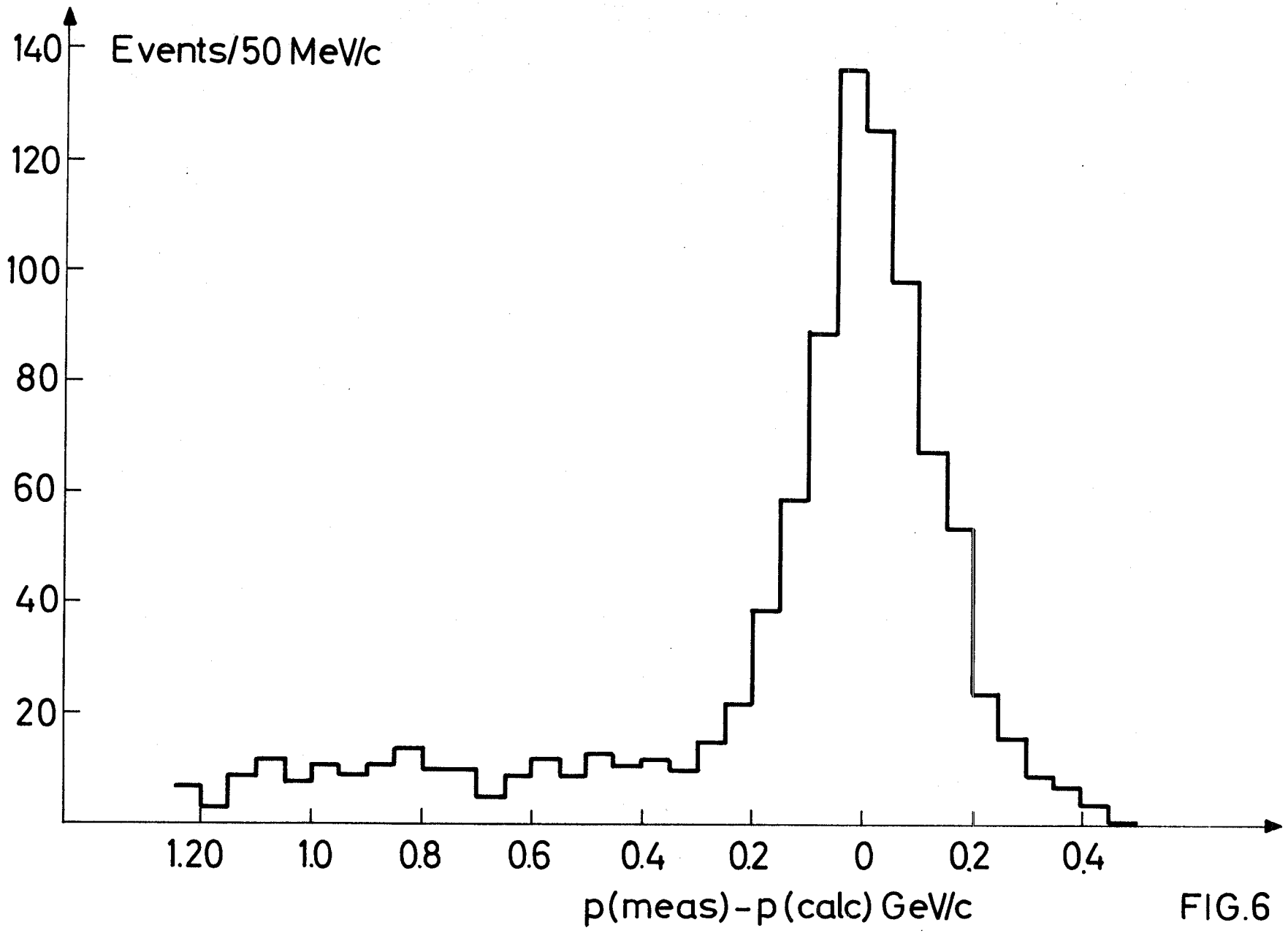
Events/50 MeV/c
140
120
100
80
60
40
20
1.20
1.0
0.8
0.6
0.4
0.2
0
0.2
0.4
p(meas)-p(calc) GeV/c

FIG.6

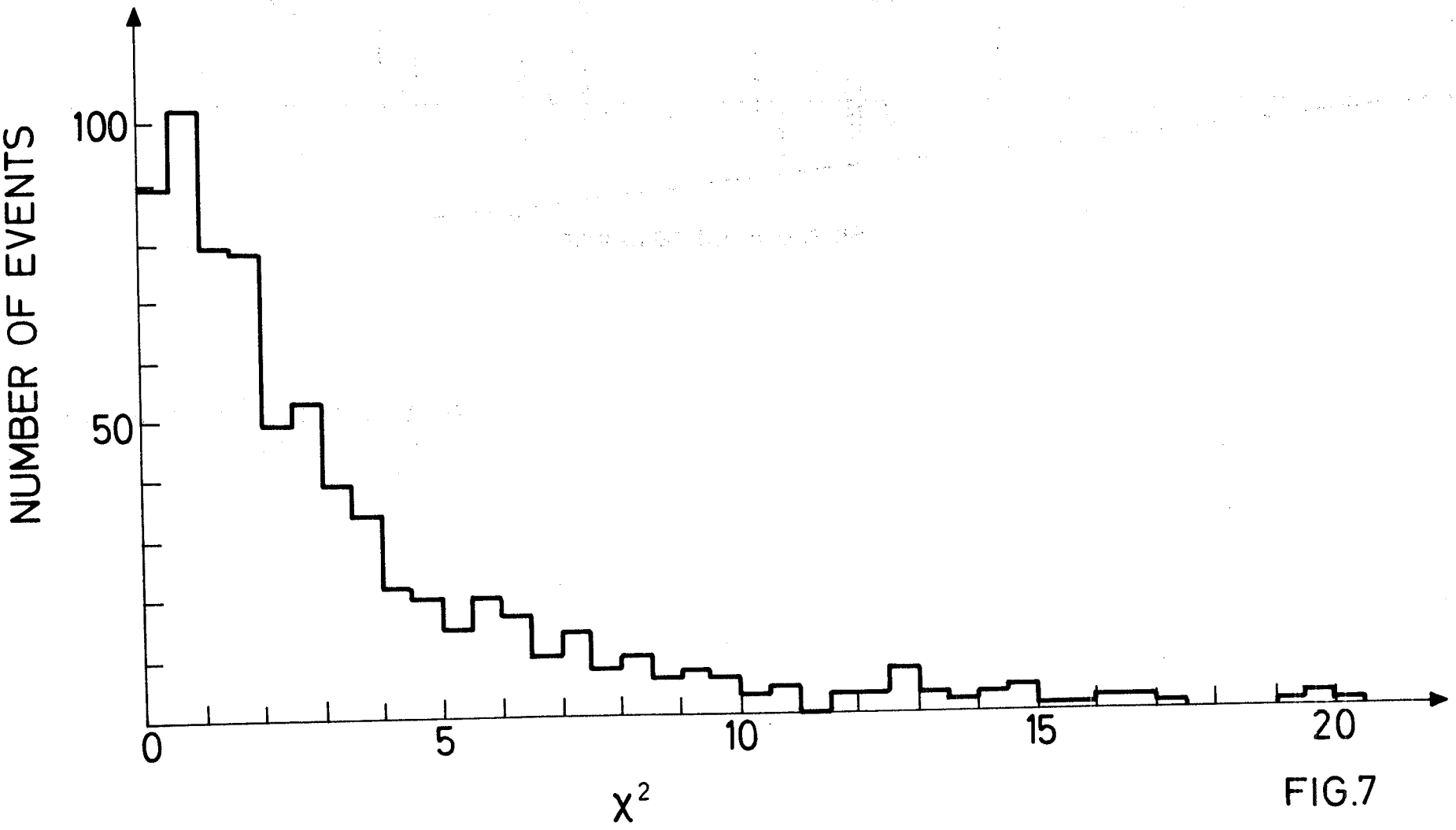

FIG.7

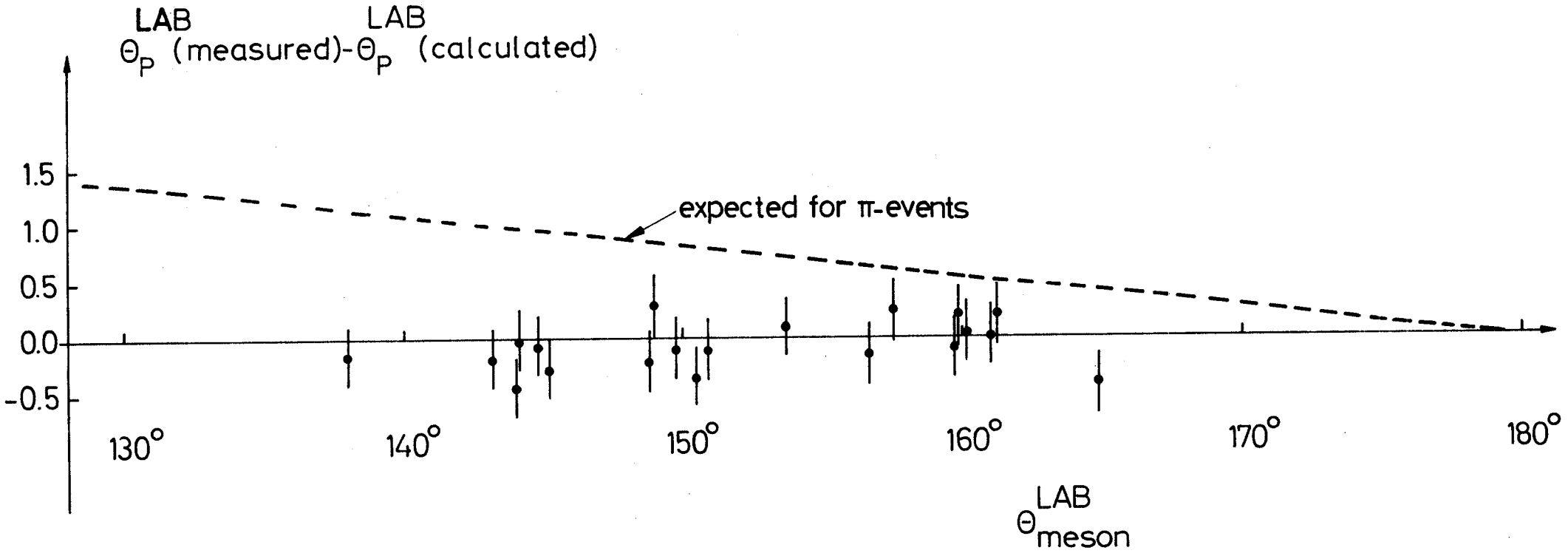
LAB
Θ_P (measured)-Θ_P LAB (calculated)
1.5
1.0
0.5
0.0
-0.5
expected for π-events
130°
140°
150°
160°
170°
180°
Θ^{LAB}_{meson}

FIG.8

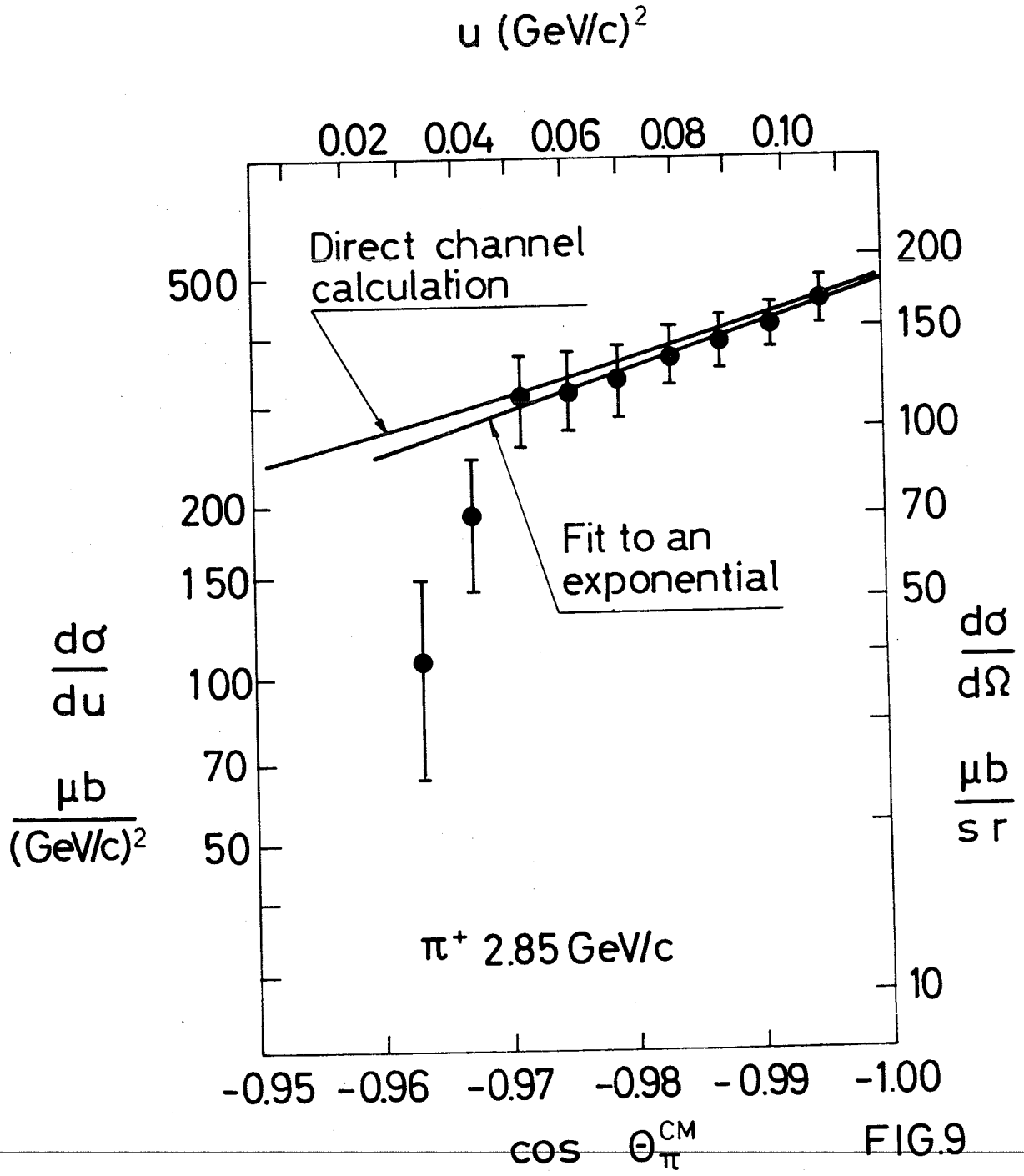
u (GeV/c)²
0.02
0.04
0.06
0.08
0.10
Direct channel calculation
Fit to an exponential
500
200
150
100
70
50
200
150
100
70
50
10
dσ/du
μb/(GeV/c)²
dσ/dΩ
μb/sr
π⁺ 2.85 GeV/c
-0.95
-0.96
-0.97
-0.98
-0.99
-1.00
cos Θ_π^CM

FIG.9

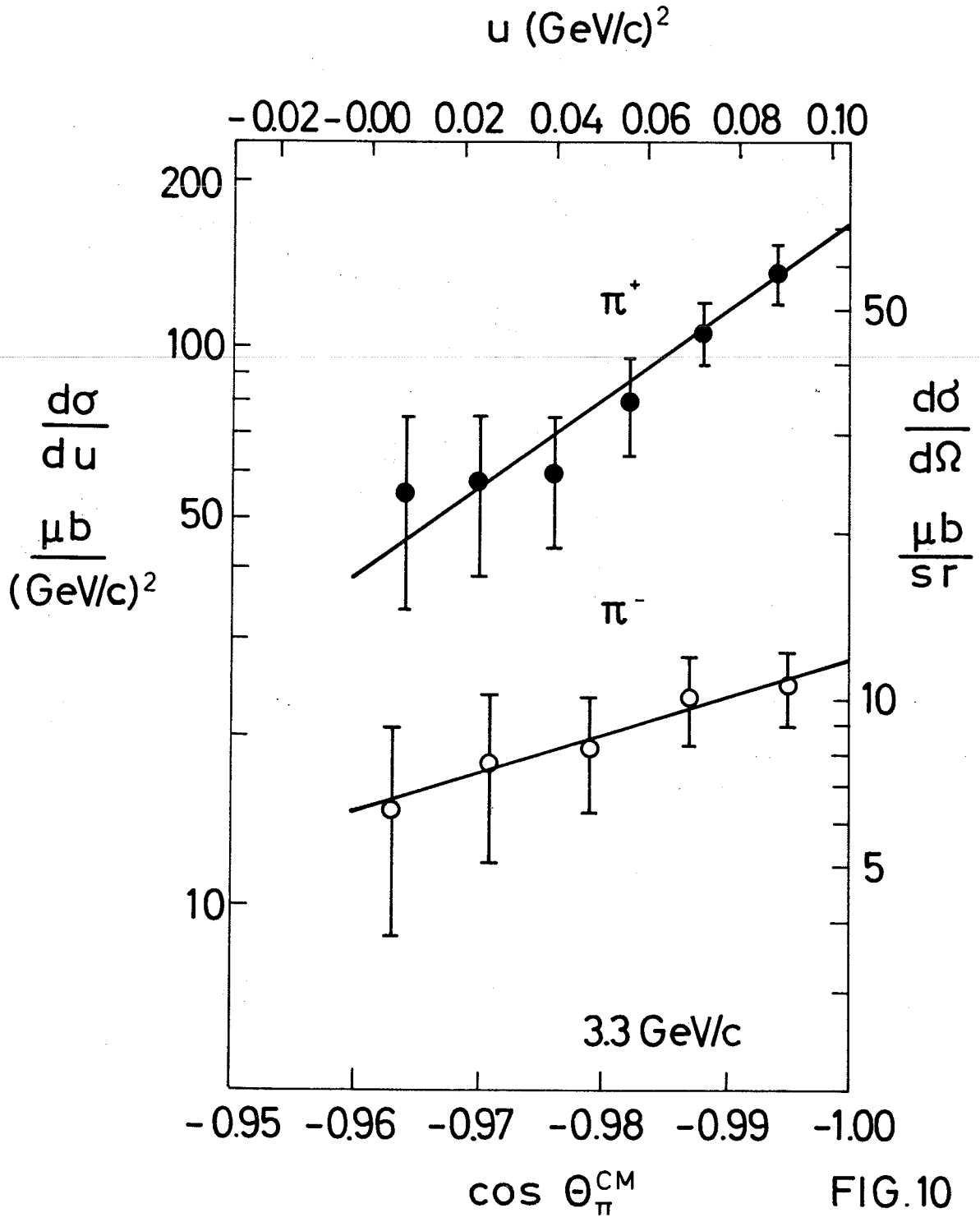
u (GeV/c)²
-0.02 -0.00 0.02 0.04 0.06 0.08 0.10
200
100
50
10
dσ/du μb/(GeV/c)²
π⁺
π⁻
50
10
5
dσ/dΩ μb/sr
3.3 GeV/c
-0.95 -0.96 -0.97 -0.98 -0.99 -1.00
cos Θ_π^CM

FIG. 10

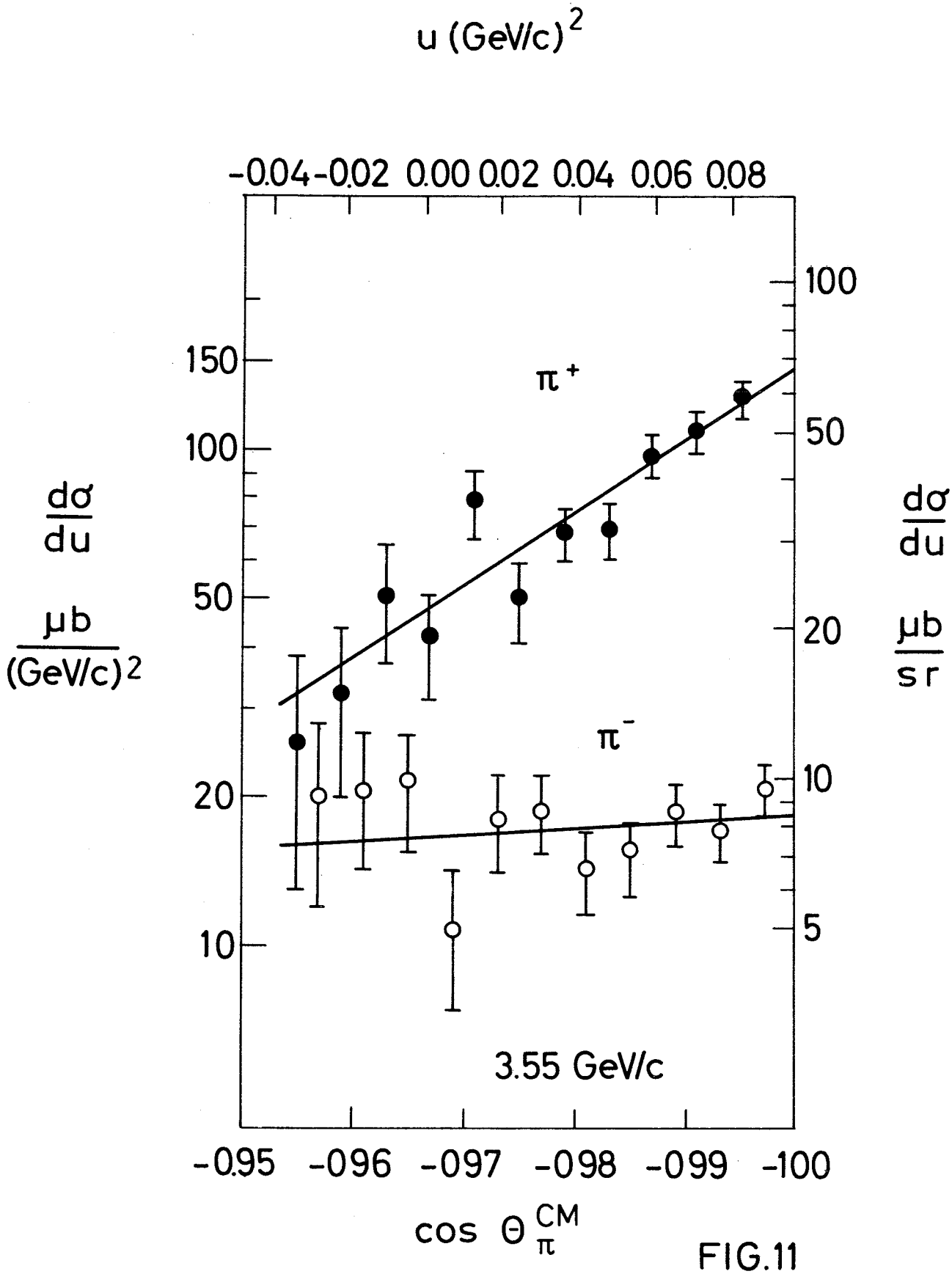
u (GeV/c)²
-0.04 -0.02 0.00 0.02 0.04 0.06 0.08
150
100
50
20
10
100
50
20
10
5
π⁺
π⁻
3.55 GeV/c
-0.95 -096 -097 -098 -099 -100
cos Θ π CM
dσ/du
μb/(GeV/c)²
dσ/du
μb/sr

FIG.11

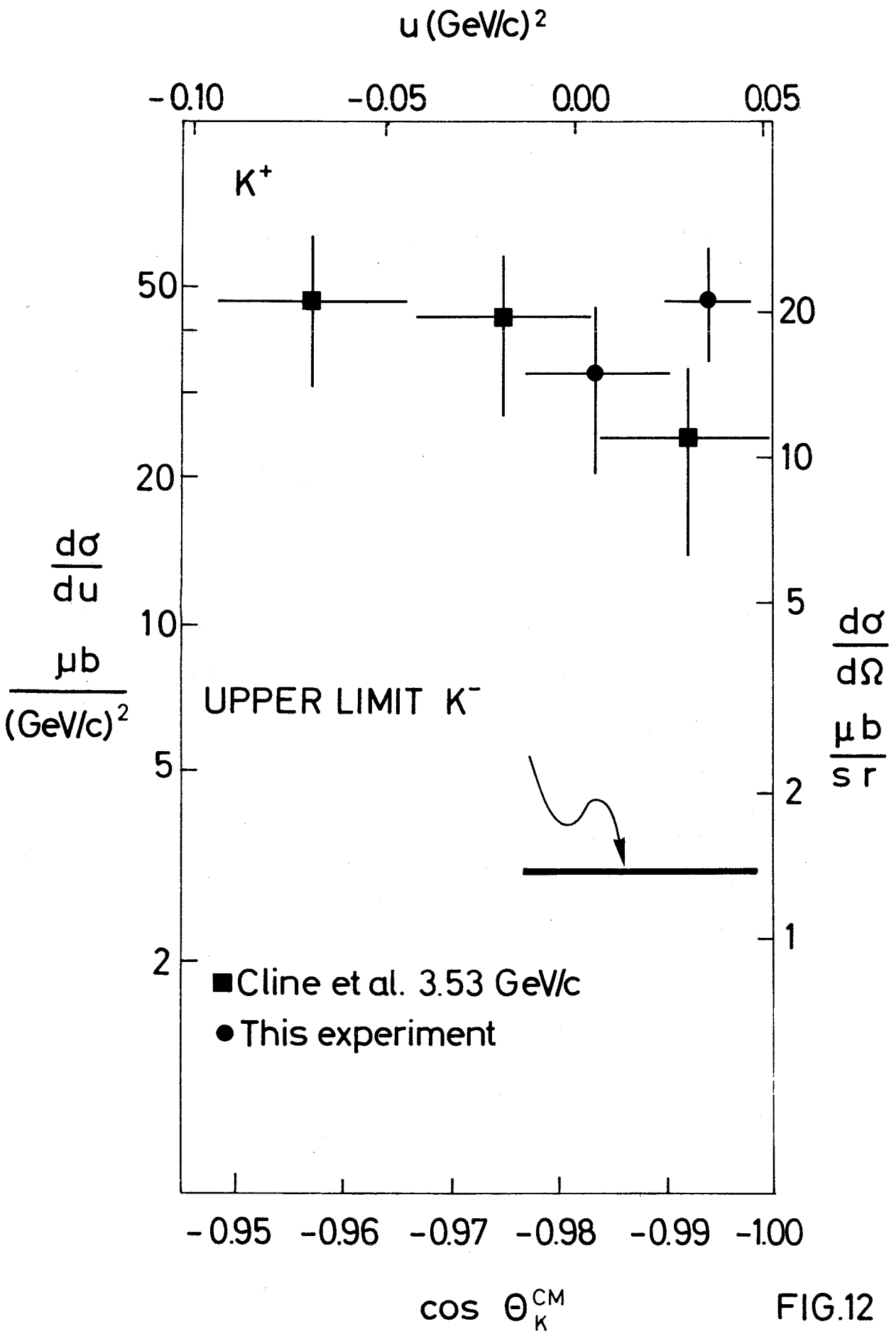
u (GeV/c)²
-0.10
-0.05
0.00
0.05
K⁺
50
20
10
5
2
20
10
5
2
1
dσ/du
μb/(GeV/c)²
dσ/dΩ
μb/sr
UPPER LIMIT K⁻
■Cline et al. 3.53 GeV/c
●This experiment
-0.95
-0.96
-0.97
-0.98
-0.99
-1.00
cos Θ_K^CM

FIG.12

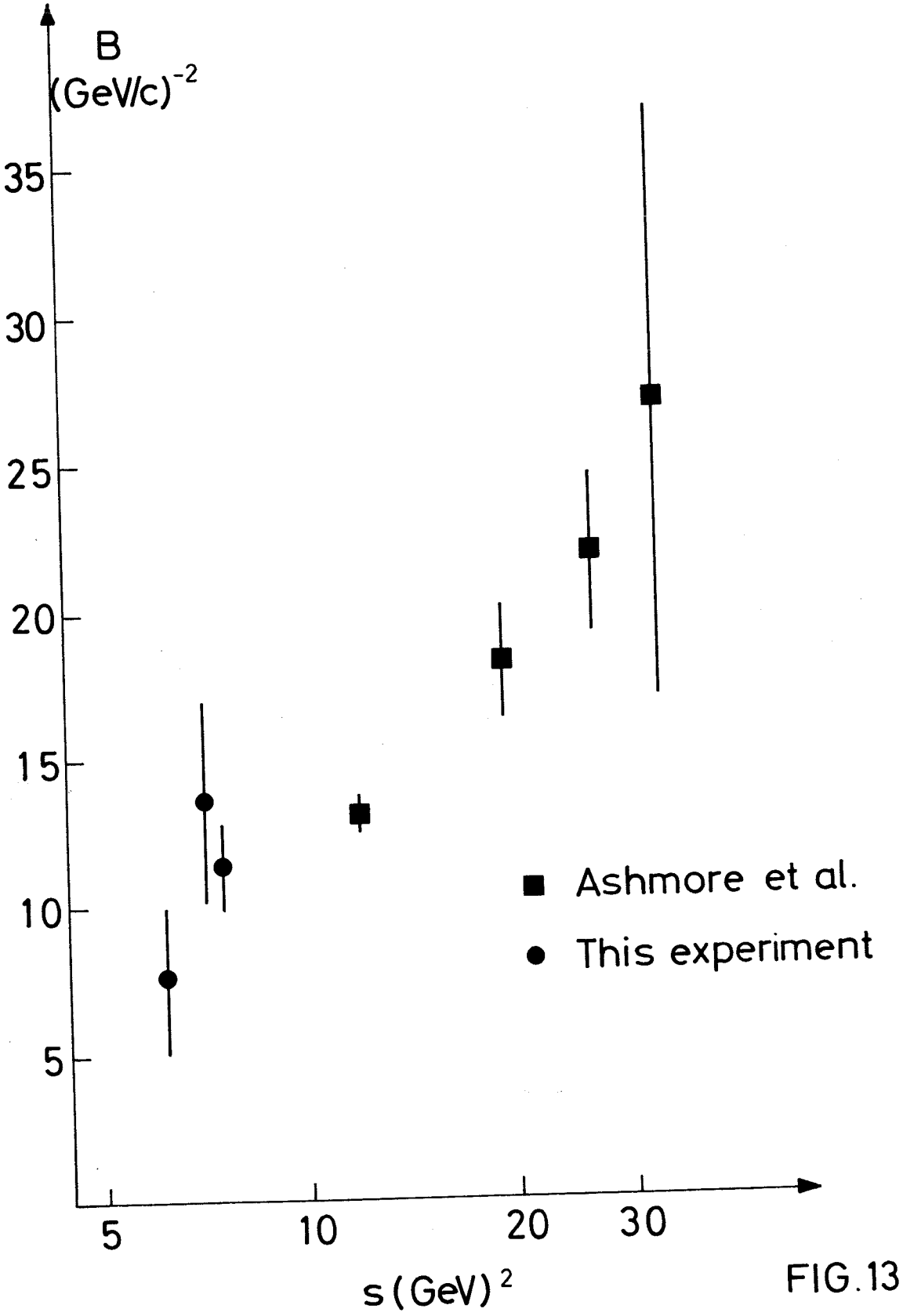
B
(GeV/c)$^{-2}$
35
30
25
20
15
10
5
5
10
20
30
s (GeV)^2
Ashmore et al.
This experiment

FIG.13

Direct channel

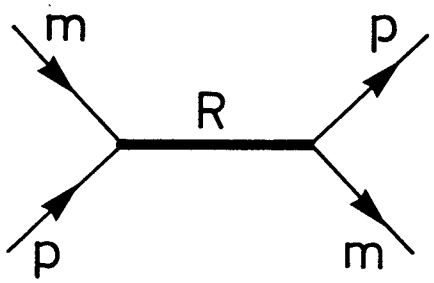

Crossed channel

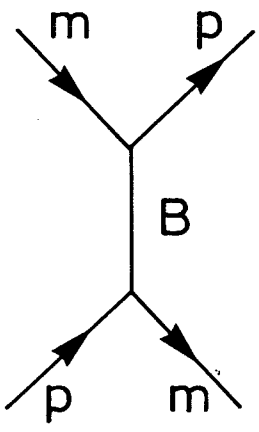

FIG.14